Structure and defect identification at self-assembled islands of CO_2 using scanning probe microscopy

Oscar Custance,*,† Emiliano Ventura-Macias,‡ Oleksandr Stetsovych,¶ Carlos Romero-Muñiz,§ Tomoko K. Shimizu,‖ Pablo Pou,‡,⊥ Masayuki Abe,# Hironobu Hayashi,† Tadakatsu Ohkubo,† Shigeki Kawai,† and Ruben Perez*,‡,⊥

†National Institute for Materials Science (NIMS), 1-2-1 Sengen, Tsukuba, 305-0047, Ibaraki, Japan

‡Departamento de Física Teórica de la Materia Condensada, Universidad Autónoma de Madrid, 28049, Madrid, Spain

¶Institute of Physics of Czech Academy of Sciences, CukrovarnickÃą 10, Prague 6, 16200, Prague, Czech Republic

§Departamento de Física de la Materia Condensada, Universidad de Sevilla, P.O. Box 1065, 41080, Seville, Spain

‖Department of Applied Physics and Physico-Informatics, Faculty of Science and Technology, Keio University, 3-14-1 Hiyoshi, Kohoku-ku, Yokohama, 223-8522, Kanagawa, Japan

⊥Condensed Matter Physics Center(IFIMAC), Universidad Autónoma de Madrid, 28049, Madrid, Spain

#Graduate School of Engineering Science, Osaka University, 1-3 Machikaneyama, Toyonaka, 560-0043, Osaka, Japan

E-mail: custance.oscar@nims.go.jp; ruben.perez@uam.es

Abstract

Understanding how carbon dioxide (CO_2) behaves and interacts with surfaces is paramount for the development of sensors and materials to attempt CO_2 mitigation and catalysis. Here, we combine simultaneous atomic force microscopy (AFM) and scanning tunneling microscopy (STM) using CO–functionalized probes with density functional theory (DFT)–based simulations to gain fundamental insight into the behavior of physisorbed CO_2 molecules on a gold (111) surface that also contains one-dimensional metal-organic chains formed by 1,4-phenylene diisocyanide (PDI) bridged by gold (Au) adatoms. We resolve the structure of self-assembled CO_2 islands, both confined between the PDI–Au chains as well as free-standing on the surface, and reveal a chiral arrangement of CO_2 molecules in a windmill-like structure that encloses a standing-up CO_2 molecule, and other foreign species existing at the surface. We identify these species by the comparison of height-dependent AFM and STM imaging with DFT calculated images, and clarify the origin of the kagome tiling exhibited by this surface system. Our results show the complementarity of AFM and STM using functionalized probes, and their potential, when combined with DFT, to explore greenhouse gas molecules at surface supported model systems.

Introduction

Carbon dioxide (CO_2) is a linear molecule with two carbon oxygen double bonds (C=O), which are responsible for its great chemical stability. In its gas form, CO_2 is transparent to visible light but strongly absorbs infrared radiation, acting as one of the main greenhouse gasses. The catalytic transformation,[1,2] capture,[3] process,[4] and utilization and removal[5] of CO_2 have attracted considerable attention for the production of liquid fuels[6,7] and the pursue of a low-carbon economy and net-zero emissions.[8] Fundamental understanding of how CO_2 interacts with surfaces is paramount to attain efficient designs of materials suitable for CO_2 catalysis and mitigation. Accurate and direct information about how CO_2 interacts with surfaces can be obtained by using carbon monoxide (CO) functionalized scanning probe microscopy[9]. [10] The deflection of the relatively chemically inert CO at the probe apex has proven to be key to enhance the resolution of both AFM[9,11–13] and STM,[14–24] enabling achieving structural intramolecular imaging,[9] the visualization of frontier orbitals,[11] the determination of bond order potentials,[25] charge distributions,[26–28] as well as to track and control chemical reactions,[29,30] boosting the field of on–surface synthesis.[31]

An interesting surface system to study the behavior of CO_2 is the one composed by the low temperature condensation of CO_2 in the presence of one-dimensional metal-organic chains formed by 1,4-phenylene diisocyanide (PDI) bridged by gold (Au) adatoms.[32–36] For a relatively large dosing of CO_2 on a surface containing PDI–Au chains, a great variety of ordered structures initially related to the high-pressure CO_2 face-centered rhombic phase —rather than to the common cubic "dry ice" phase— have been identified using STM.[35,36] STM revealed the presence of both rhombic and hexagonal structures within CO_2 islands that grow close to the PDI-Au chains.[35,36] In the areas with sparse PDI–Au chains, domains of hexagonal defects of unknown nature with a kagome tiling that penetrates the rhombic structures were reported.[35,36] In this work, we provide a new perspective on this surface system by studying it with a combination of STM and AFM with CO-functionalized probes.[9] The intramolecular resolution offered by these techniques allows us to determine the molecular structure of the self-assembled CO_2 islands and to identify an arrangement of physisorbed CO_2 molecules that relates to the intrinsic defects of the surface system. The simultaneous application of AFM and STM, both in the experiments and the simulations, enables us to address the nature of structures that would have been unresolved by using only one of these techniques.

Results and discussion

The room-temperature deposition of a small amount of PDI molecules (Figure 1a) on an atomically clean surface of a Au(111) single crystal produces dispersed PDI–Au chains[32–34] that nucleate from the lower part of a step edge towards the terraces (Figure S1a). STM topographic imaging presents the PDI-Au chains as bright strings formed by round and oval beads (Figures 1b and S1a). If CO_2 is dosed after cooling down the sample to 4.8 K, the CO_2 molecules decorate the PDI-Au chains (Figures 1b and S1a).[37] In topographic STM images, the CO_2 molecules appear as round protrusions close to the chains (Figure S1a) or around CO molecules (Figures S3 and S4). The interaction of the CO_2 molecules with the PDI–Au chains is limited to the first (in some locations to the second) line of molecules (Figure 1c), from which the CO_2 starts to grow following its native adsorption structure on the Au(111) surface forming of an apparent rhombic periodicity of protrusions (see the rhombic lattices in Figure 1c).[36] Nucleation of CO_2 at different positions along the chains (Figure S1) produces patches of different translational domains (Figure 1g).

AFM imaging of the surface with CO-functionalized probes displays sub-molecular resolution on the PDI, as well as on the CO_2 molecules (Figure 1d). The toroidal shape of the phenylene group of the PDI and the isocyanide (N≡C) groups connecting to the Au adatoms[38] are clearly visible (Figures 1d and 1g). The AFM shows that the CO_2 molecules arrange in a herringbone pattern (Figure 1d). Similar to the AFM imaging of water networks on metal surfaces,[39] the CO probe seems to sense the position of the oxygen atoms, giving rise to the two lobes of the dumbbell-like shape exhibited by the CO_2 molecules(Figure 1d). Since the AFM senses atomic arrangements[9] rather than the electronic structure,[40] slight variations in the height of identical atomic species are immediately detected.[41] Our AFM data indicate that the CO_2 molecules lie flat and parallel to the surface, following the topography of the underlying substrate, as a modulation of the images induced by the herringbone reconstruction of the Au(111) surface is observed in both the STM and the AFM signals (Figures 1f, S2 and S3).

Defective areas are found between domains of CO_2 molecules. In these areas, some CO_2 molecules present a triangular arrangement (white triangles in Figure 1c). There are three types of defects populating the layer of CO_2 between the PDI-Au chains. Voids can be found between the CO_2 domains as well as at the frontiers with the PDI-Au chains (green arrows in Figure 1f). They are characterized by no apparent signal either in STM or AFM.

Single and double lines of defects appear between the CO_2 domains (orange arrows in Figure 1f). In the STM images, these defects are perceived as depressions (Figures 1f and 1g), and they are forming the kagome tiling reported for this surface system.[35,36] The AFM contrast for these defects considerably varies with the probe-surface separation. A strong attractive interaction is detected at distances where there is barely contrast over the PDI or the CO_2 molecules (Figure 1e). A repulsive interaction is sensed at distances at which the interaction over the PDI and the CO_2 layer starts to be attractive (Figure 1f). At distances where the onset of the repulsive interaction over the PDI and the CO_2 layer is observed, the contrast over the defects is strongly repulsive (Figure 1g). These defects are also found individually distributed between smaller domains of CO_2 molecules, as it is shown in the upper part of the AFM images displayed in Figures 1e to 1g.

Finally, another defect that is found between the CO_2 domains is indicated by yellow arrows in Figure 1f. This defect appears as a vacancy in the STM signal, and it is practically invisible to the AFM (Figures 1e and 1f). Only upon scanning at very close distances the defect enclosed by the CO_2 molecules is revealed (Figure 1g). From control experiments we have done without PDI molecules (see FiguresS3 and S4), this type of behavior would be associated with a CO molecule trapped in the CO_2 layer.

Excluding the voids, the defects detected in the CO_2 layers seem to be trapped inside hexagonal structures (Figures 1c and 1h), which are related to the CO_2 molecules displaying a triangular arrangement in Figure 1c. When scanning close enough to the surface using a probe functionalized with a CO molecule,[9] the deflection of the CO along the bonds of the molecules enhances the STM contrast.[15,18,20] This effect can be appreciated in the image displayed in Figure 1h: the STM signal over the CO_2 is no longer homogeneously round (as in Figure 1e) but it exhibits a brighter region that coincides with the orientation of the CO_2 molecule in the AFM image (Figures 1h and 1g). The bond-resolved STM signal of the CO_2 molecules surrounding the defects indicates that the CO_2 seems to arrange in a *windmill*-like configuration (Figure 1h).

The CO_2 structures and defects described in Figure 1 are not intrinsic to the confinement of the CO_2 molecules between the PDI–Au chains, but they are inherent to the behavior of the CO_2 on the surface, as they are also observed at islands of CO_2 molecules nucleated at the middle of the Au(111) terraces upon the presence of a relatively high-concentration of CO at the surface (Figures S1 and S3 to S5). Figure 2 displays a selection of frames from a series of simultaneously acquired constant height STM and AFM images recorded over a total of 68 pm distance variation in steps of 4 pm over an island of CO_2 molecules on the Au(111) surface. This island was found on a sample in which PDI molecules were also present (Figure S1), and it was specially chosen because it contains the three types of defects (labelled as **P**, **S** and **A** in Figure 2d) also observed at the confined CO_2 layers between PDI–Au chains. The AFM measurements over this island confirm the molecular arrangement of the windmill-like structure (see Figures 2c and 2g) predicted by bond-resolved STM imaging that enclose the defects observed at the CO_2 layer (Figure 1h).

At the starting distance of the series, the AFM signal mainly corresponds to a long-range van der Waals interaction, which produces a faint contrast difference between the CO_2 island and the gold surface (Figure 2a). Already at this separation, similarly to the image in the Figure 1e, the **P** defect shows a strong attractive force signal that becomes repulsive by approaching the probe towards the surface (Figures 2b and 1f), and develops into a pinhole when further reducing the gap (Figures 2c and 2d). The appearance of a pinhole and the increase of contrast over the surrounding CO_2 molecules forming the windmill-like structure suggest a significant deflection of the CO molecule at the probe or a considerable mobility of the **P** defect. The STM signal for the **P** defect evolves from a faint contrast similar to the

CO_2 molecules of the island (see movie at the Supporting Information) to a total depletion of tunneling current (Figures 1g and 2f) at the closest approach.

The **S** defect appears as a vacancy in the STM images (see movie at the Supporting Information and Figure 1e). Only at the closest approach some contrast is observed inside the windmill-like structure of CO_2 enclosing it (Figure 1h and Figure 2f). In the AFM images, the **S** defect is seen as a blurry hexagonal spot up to distances at which the CO_2 forming the island starts to be resolved (Figure 2b), and it develops into a clear round shape of size comparable to the surrounding CO_2 molecules, but with a slightly lower signal (Figures 1g, 2c and 2d). This contrast difference indicates that the species inside the windmill-like structure either interacts less with the probe than the CO_2 layer or that it is located below the plane defined by the CO_2 molecules.

The **A** defect appears in the STM images as a bright spot (see movie at the Supporting Information) that dominates the signal detected over the whole island for shorter separations (Figure 2e). The AFM signal over the **A** defect initially resembles that of an **S** defect (Figures 2b), but it develops into a strong attractive interaction force perceived as a dark spot (Figure 2d) located at the position where the tunneling current is maximum (Figure 2e).

The behavior of the **P** defect in the AFM images is that of an object protruding from the surface well above the plane formed by the CO_2 layer, yet the conductivity through this object should be low enough to resemble a vacancy in the STM images. A hypothesis that embraces these attributes is a CO_2 molecule standing up on the Au(111) surface confined within the windmill-like structure. From control experiments we performed dosing with CO_2 and CO molecule in the absence of PDI molecules on the surface (Figures S3 and S4), the **S** defect should correspond to a CO molecule surrounded by a windmill-like structure of CO_2 molecules. The **A** defect could correspond to a gold adatom confined by CO_2 molecules in a windmill-like configuration, as the underlying position of this defect is an elbow of the Au(111) herringbone reconstruction; a well-known surface spot for the nucleation of metallic adatoms.[42] The lower resistivity and closer position to the surface of a gold adatom with respect to the CO_2 molecules would account for the high tunneling current signal and the attractive force detected on the defect.

We used DFT calculations to optimize the structures observed and corroborate the nature of the defects, considering a windmill arrangement as a baseline for the latter, as suggested by the experiments. The charge density, electrostatic potential, and wave functions resulting from these calculations are used to simulate AFM and STM images,[43,44] including the relaxation of the CO at the probe and proper tunneling channels (see Methods), that can be directly compared with the experimental counterparts.

The geometry of the herringbone pattern of CO_2 is shown in Figure 3a. The unit cell of the herringbone order —gray orthorhombic cell in Figure 3a— has one molecule tilted to the right $\sim 58^\circ$ from the horizontal axis, and another molecule symmetrically tilted to the left. Our DFT simulations confirmed the stability of the herringbone pattern of CO_2 on the Au(111) surface (Figure S7), and the associated theoretical AFM images further support the experimental AFM data (see Methods and Figures S8 and S9). In the presence of an open space, a CO_2 molecule can place itself close by to two CO_2 molecules of the unit cell, forming an equilateral triangular subunit (Figure 3b), for which the repulsion between the oxygen atoms of the three molecules is balanced. These formations are observed in the experiments, see the triangular structures in Figures 1c, 2h and 2g. The local arrangement of three triangular subunits produces a windmill-like structure that naturally generates a free space between the molecules (Figure 3c). Although an empty windmill structure has not been observed in the experiments, our DFT calculations confirm that this formation is stable on the Au(111) surface (Figure 3d). A gold adatom confined inside a windmill sits on a hollow-*hcp* site, 150 pm below the CO_2 molecular layer layer and 190 pm above the unreconstructed Au(111) surface (Figure 3e). A standing CO_2 adsorbs vertically with an O atom sitting between a hollow-*hcp* and a top site 290 pm above the surface, with its top O atom protruding $\sim$ 190 pm from the molecular layer, and sustaining a small tilt of $\sim 10^\circ$ (Figure 3f). A CO molecule also adsorbs vertically with the C atom 210 pm above an Au top site, and the O atom 10 pm below the CO_2 molecular layer (Figure 3g).

Figures 4a to 4d show AFM images of the atomic configurations obtained from DFT, calculated for separations between the oxygen atom of the CO molecule at the probe and the CO_2 molecular plane of 357 pm, 326 pm, 311 pm, and 280 pm. In Figures 4e to 4h, calculated STM images at 311 pm separation are presented. The rows of images labelled as *relaxed* and *static*, include and obviate, respectively, the relaxation of the CO molecule at the probe. The rows of images considering the tunneling through both the 5σ and the $2\pi^*$ orbitals (represented by the s and the p_x, p_y orbital channels, see Methods) of the CO molecule at the probe are labelled as *sp*-channel. The comparison with images considering only the *s–channel* for the calculation of the tunneling current (rows labelled as *s–channel*) shows that both channels contribute significantly and are necessary to explain the observed experimental contrast. The empty space enclosed by the windmill shows values for the calculated AFM and STM images close to the ones obtained over the gold substrate. A less attractive AFM force inside the windmill is due to the interaction of the CO molecule at the probe with the oxygen atoms of the surrounding CO_2 molecules (the ovals in Figures 3d and 4a to4d highlight one of these molecules). The AFM signal over the planar CO_2 is stronger over the oxygens than the carbon atom. While the Pauli repulsion is similar for both species, the carbon has a larger electrostatic attraction (Figures 4a to 4d). For large probe–surface distances, the charge density is dominated by the oxygen atoms. At a separation of ∼326 pm, the short-range repulsion over the carbon atoms overcomes the electrostatic attraction, developing into a faint feature that connects the two oxygen atoms of the CO_2. At closer distances, the short-range repulsion dominates the contrast, and the relaxation of the CO probe becomes significant. In particular, the probe relaxation lowers the signal measured over the oxygens, resulting in an image that displays each CO_2 molecule as a homogenous rod. This contrast evolution can be clearly seen over the CO_2 molecules composing the windmills in the experimental AFM images of Figures 2c and 2d, as well as in the theoretical simulations (Figure S9).

The STM images (Figures 4e to 4h) are dominated by a molecular state that extends along the bonds of the CO_2, displaying it as an oval centered on the carbon atom. At small probe-layer separations, a repulsive interaction with the oxygen atoms of the CO_2 molecules deflects the CO at the probe, reducing the STM contrast over the oxygen atoms. This effect transforms the oval STM signal at large separations to a sharp-edged feature along the long molecular axes at the closest approach —compare Figures 4e and 4g (static) with Figs 4f and 4h (relaxed). The contrast mechanism for both STM and AFM images is identical for the planar CO_2 forming the molecular layer between the PDI–Au chains.

The gold adatom (Figure 3b) presents a similar behavior in the AFM signal as for an empty windmill (Figures 4a to 4d). The onset of a Pauli repulsion with the inner oxygen atoms of the windmill is the origin of the blurred AFM contrast observed at far enough separations (Figure 2b). The characteristic signature of the gold adatom is a strong STM signal (Figures 4e to 4h) for all the separations explored (Figure S11), as it helps the electronic states of the substrate to extend out through the CO_2 molecular plane.

Since the standing CO_2 inside the windmill protrudes from the molecular plane, a strong repulsive AFM contrast is already obtained at distances where no significant signal is detected on the molecular layer (Figure 4a). This contrast disappears at closer probe-layer separations (Figures 4c and 4d) because of the small oscillation amplitude used. Simulations show that the standing CO_2 has a dimmer contrast for smaller amplitudes (Figure S10), consistent with the ∼75 pm amplitude used in the experiments. This effect comes from a change in interaction force mainly due to the deflection of the CO molecule at the probe.[45] Further DFT simulations of a CO probe (attached to a copper dimer) approaching the standing CO_2 in the windmill show that the CO deflects ∼15° while the CO_2 tilts only ∼2° when reducing the separation from 300 pm to 270 pm. The relaxation of the CO molecule at the probe is also responsible for a STM signal over the standing CO_2 as low as for the gold substrate (images labelled as (*relaxed*) in Figures 4f and 4h). If the tilting of the CO molecule at the probe is not taken into account, the STM images show the trapped CO_2 as a bright spot (images labelled as (*static*) in Figures 4e and 4g), which is also the appearance for separations at which the CO molecule at the probe does not significantly relax.

The calculated AFM signal over a CO molecule inside a windmill (Figures 4a to 4d) resembles the one over a free CO on a metal substrate,[46,47] but the confinement imposed by the surrounding CO_2 molecules prevents its relaxation, making the AFM contrast sharper upon reducing the probe-layer distance. As in the Au adatom case, the initial blurred contrast (Figure 2b) is due to the interaction with the inner oxygen atoms of the windmill. At closer distances (below 326 pm, Figures 4b to 4d), a white spot in the center of the windmill reveals the presence of a repulsive interaction between the two oxygen atoms, one at the adsorbed CO molecule and the other at the approaching CO with the probe. The STM images of the enclosed CO molecule come from states spreading out from the gold surface more than that of the CO_2 molecular layer. These images present the CO as a fully symmetric faint spot at the center of the windmill, consistent with a molecular adsorption in a vertical configuration. Far from the surface, the STM contrast over the CO is weaker than the one over the planar CO_2 because of the lower position of the CO with respect to the molecular layer, but the difference in contrast reduces at closer separations due to the deflection of the CO molecule at the probe (Figure S11).

The resemblance of the experimental and calculated features in both the AFM and the STM images (Figure 5) allows us to unambiguously identify the defects trapped inside windmill structures at the CO_2 layers as a gold adatom (defect **A** in Figure 2d), a standing up CO_2 molecule (defect **P** in Figure 2d and orange arrows in Figure 1f) and a CO molecule (defect **S** in Figure 2d and yellow arrows in Figure 1f).

Considering the clear experimental evidence of the presence of windmill structures at the CO_2 layers, we attempted to generate them through DFT calculations. Initially, we tried large commensurate periodic structures of CO_2 molecules on the unreconstructed Au(111) surface (including up to 50 molecules in the unit cell), but this planar herringbone configuration of CO_2 was unstable under the creation of a vacancy by removing one molecule from the structure. We then considered an island of planar CO_2 molecules adsorbed on the unreconstructed Au(111) surface (see Figure S7 for a discussion of the geometrical details and the stability of all of these structures). However, neither the removal of one CO_2 molecule of the layer, nor the introduction of a gold adatom or a standing CO_2 molecule or a CO molecule inside the created vacancy, resulted in a stable structure with the chiral pattern observed for the windmill. These results, together with dynamic processes observed during the experiments (see Figure S5) provide clear evidence of the formation of the windmills during the growth of the CO_2 layer. In particular, consecutive STM images in Figures S5b and S5c capture the real-time formation of a windmill-like structure around a CO molecule in a CO_2 island.

The analysis of the molecular arrangement of both the monolayer of CO_2 molecules trapped between PDI-Au chains (Figure 1c) and the island on the terrace (Figures 2f and 2g) offers insights on the windmill formation. The planar CO_2 molecules are weakly bound to the surface and, due to intermolecular interactions, they tend to order under a rhombic pattern with a herringbone arrangement, which is the native structure of CO_2 adsorbed on the Au(111) surface (see FiguresS2 and S3). Under the presence of adsorbates, such as a gold adatom of a CO molecule, the triangular structure depicted in Figure 3b is formed by accommodating CO_2 molecules to the sides of the unit cell of the herringbone structure around the adsorbate (see FigureS5). Thus, these triangular structures are often found at the edges of the CO_2 islands (Figures 2f and 2g).

Triangular arrangements giving rise to lines and double lines of windmill structures (aligned white hexagons in Figures 6a and 6b) are commonly found at the confluence between herringbone molecular domains (Figures 1c, 2f and 2g). These domain boundaries are formed by the growth of CO_2 domains at different nucleation points on the gold terraces or along the PDI–Au chains. Details of the molecular arrangement of such domain boundaries are shown in Figures 6c and 6d. Lines of windmills containing standing CO_2 molecules result from the confluence of two domains translated by half of the short lattice parameter and a quarter of the long lattice parameter of the rhombic unit cell (Figure 6c). Domains displaced only in the direction of the long lattice parameter can form a boundary with two rows of windmills, as depicted in Figure 6d. It is straightforward to note that the CO_2 molecules at the corners of the cells of the domains (highlighted with arrows in Figures 6c and 6d) have moved and rotated to form a triangular arrangement to optimize the interaction with the neighboring molecules. Building on the defect identification (Figures 4 and 5), the strong repulsive interaction detected at the center of the windmills in the AFM image (Figure 6b) indicates that they contain standing CO_2 molecules. The molecules at the corners of the unit cell of the domains highlighted with a circle in Figures 6c and 6d become the CO_2 molecules standing up at the center of the windmills enclosed by the white hexagons. The nearby windmills observed in Figures 6a and 6b have a similar origin, and they also contain standing CO_2 molecules, except two of them that contain a CO molecule (hexagons without a bright feature in 6b). Although both defects have a very similar STM contrast (Figure 6a), AFM clearly discriminates between them, highlighting the need to combine both signals to achieve complete identification. These CO molecules are incorporated in the domains of CO_2 molecules because a small amount of CO was also dosed on the surface to functionalize the probe (see Methods). CO_2 can diffuse on the surface upon dosage and nucleate around the CO (see FigureS5). We have shown that the standing CO_2 molecules populating these rows of windmills are imaged as dark spots in the STM signal (Figures 1g, 2f and 5b). The confluence of domains and the formation of linear arrangements of windmill structures containing vertical CO_2 molecules are the origin behind the Kagome tiling reported by Feng et al.[35,36]

Conclusion

We have shown how the combination of simultaneous AFM and STM imaging using CO-functionalized probes[9] with DFT-based simulation tools for both techniques provide a comprehensive description of the ordered structures and defects found in CO_2 layers confined between PDI–Au chains and islands found at the terraces of the Au(111) surface. CO-functionalization of the probe[9] increases the resolution and enables the determination of the orientation of individual CO_2 molecules and the visualization of complex structures around defects. The native adsorption configuration of CO_2 on the Au(111) surface is in the form of a planar molecular layer following a rhombic lattice displaying a herringbone pattern that is controlled by intermolecular interactions. This characteristic, together with a weak interaction with the substrate, makes the CO_2 molecular layer non-commensurate with the gold surface, even for the large periodicities that we have explored. Our data suggest that the PDI-Au chains capture the CO_2 molecules diffusing on the surface all along the chain, and that the interaction of the CO_2 molecules with the PDI-Au chains is mostly limited to the first line of CO_2 molecules, growing in its native adsorption configuration on the Au(111) surface after the second molecular line.

At the edge of molecular islands growing at the terraces, and at the boundaries of the CO_2 herringbone domains, the formation of triangular arrangements of CO_2 molecules is observed. The combination of these triangular formations and the terminations of the herringbone domains lead to the formation of a windmill structure. Defects enclosed by these windmills display characteristic signatures in the experimental STM and AFM images, reproduced by first-principles simulations that include the relaxation of the CO at the probe and the 5σ and the $2\pi^*$ CO orbitals as tunneling channels. In this way, gold adatoms, CO and CO_2 molecules standing up on the gold surface enclosed by windmill structures have been identified. These standing CO_2 molecules populate windmills along domain boundaries, giving rise to the formation of the previously reported Kagome tiling for the confinement of CO_2 molecules by one-dimensional PDI–Au organometallic chains.

Our results strengthen the complementarity of simultaneous AFM and STM imaging using functionalized probes and show the potential of these techniques to study the adsorption and behavior of greenhouse gasses at model surface systems. This work reaffirms that the excellent resolution offered by combining AFM and STM using functionalized probes has the potential to significantly contribute to current challenges where atomic-scale information is of the essence, including the development of nanocatalysts, on–surface synthesis and supramolecular chemistry.

Methods

Scanning probe microscopy experiments

The experiments were carried out in an ultra-high vacuum (UHV) system equipped with tools for the *in situ* sample preparation and a home-made scanning probe microscope operated at 4.8 K using a commercial controller (Nanonis SPM Control System, SPECS, Germany). We used the KolibriSensor (SPECS, Germany) for the detection of both tunneling current and the probe-surface interaction forces. The probe of the KolibriSensor was sharpened to a typical apex radius of ∼15 nm *ex situ* by using a focused ion beam, and it was further conditioned for atomic resolution imaging *in situ* on a clean area of the Au(111) surface. The probe was functionalized with carbon monoxide using vertical manipulation techniques[9,48] and then used for high-resolution imaging. The bias voltage was applied to the sample. Atomic force microscopy experiments were carried out using the frequency modulation detection mode[49] keeping the oscillation amplitude constant. The surface of a Au(111) single crystal was cleaned by repeated cycles of argon ion sputtering and annealing in UHV. PDI molecules (Sigma-Aldrich) were deposited on the clean Au(111) surface by sublimation at room temperature using a home-built Knudsen cell that was differentially pumped using a turbo-molecular pump. After PDI deposition, the samples were transferred to the microscope and cooled down to 4.8 K. Prior to starting the measurements, CO and CO_2 molecules were dosed to the sample by backfilling the microscope chamber with the corresponding gas, opening the shutters of the radiation shields at the cryostat during the dosing. Typical dosage was 9 Langmuir for CO_2 and 0.4 Langmuir for CO. To prevent desorption from the surface, the dosing of both molecules was done while keeping the sample temperature below

16 K. Successive sample preparations give rise to a gradually increasing amount of CO on the surface due to desorption from nearby surfaces at the cryostat and microscope.

First–principles calculations

The DFT simulations were performed with VASP,[50] using a plane waves basis set with a cut-off of 400 eV, PAW pseudopotentials,[51] and a PBE approach[52] for the exchange-correlation potential. All complemented with Grimme's D3[53] method to account for the dispersion interactions. AFM images were simulated by using our Full Density Based Model (FDBM)[43,44] as implemented in the pyFDBM package. FDBM offers efficient calculations for frequency shift images while retaining DFT accuracy in the forces and reproduces with high-accuracy experimental images.[43–45] The application of the FDBM to the CO_2 herringbone configuration is illustrated in Figure S8. Calculations have been made with an oscillation amplitude of 69 pm and a CO_2 torsional stiffness of 0.4 eV/rad^2 (~ 0.7 N/m). The parameters α and V_0 for the description of the short-range Pauli repulsion are 1.06 and 35.16 $eV/Å^{3*(2\alpha-1)}$. To simulate STM images acquired with a CO-functionalized metal probe,[21,54,55] we used a newly implemented method in pyFDBM, that combines the Tersoff-Hamann[56] and Chen's approaches[57,58] to describe the tunneling through the 5σ and the $2\pi^*$ orbitals of the CO at the probe apex[15] with the effect of its lateral bending as described by our FDBM. The input for these simulations is a single DFT calculation for the wave functions and the charge density of each configuration of the sample system, including the Au substrate. Considering the symmetry of the 5σ and the $2\pi^*$ orbitals, they are represented by s and the p_x, p_y orbital channels. They contribute to the tunneling current through a sample wave function ψ with a term proportional to $|\psi|^2$ and $|\partial\psi/\partial x|^2 + |\partial\psi/\partial y|^2$, following Chen's proposal. The contribution of both channels is essential to reproduce the experimental images. Our calculated images are the sum of the contribution from both channels with the same weight (0.5) and include sample wave functions in a range of $+200$ meV above the Fermi level.

Acknowledgement

This work was supported by NIMS grants (AG2030 and AM2100), by several Grant-in-Aid for Scientific Research (19H05789, 21H01812, 21K18876, 22H00285, 24K01350, 24K21716) from the Ministry of Education, Culture, Sports, Science and Technology of Japan (MEXT) and by the Spanish Ministry of Science and Innovation (MCIN), through project PID2020-115864RB-I00, TED2021-132219A-I00, and the "María de Maeztu" Programme for Units of Excellence in R&D (grant No. CEX2018-000805-M and CEX2023-001316- M). O.S. acknowledges support from the Japan Society for the Promotion of Science (JSPS) under the fellowship number PE16046. C.R.-M. acknowledges financial support by the Ramón y Cajal program of the MCIN (ref. RYC2021-031176-I). The Spanish Supercomputing Network (RES) is acknowledged for providing computational resources at the Finisterrae Supercomputer (CESGA, Santiago de Compostela).

Supporting Information Available

- SI.pdf file containing Figures S1 to S11.
- IslandMovie.MP4: Movie showing the contrast evolution of the AFM and STM signals with the probe-surface separation in the island of CO_2 molecules displayed in Figure 2.

References

(1) Wang, L.; Chen, W.; Zhang, D.; Du, Y.; Amal, R.; Qiao, S.; Wu, J.; Yin, Z. Surface strategies for catalytic CO_2 reduction: From two-dimensional materials to nanoclusters to single atoms. *Chem. Soc. Rev.* **2019**, *48*, 5310–5349.

(2) Oh, Y.; Hu, X. Organic molecules as mediators and catalysts for photocatalytic and electrocatalytic CO_2 reduction. *Chem. Soc. Rev.* **2013**, *42*, 2253–2261.

(3) Yu, C. H.; Huang, C. H.; Tan, C. S. A Review of CO_2 Capture by Absorption and Adsorption. *Aerosol Air Qual. Res.* **2012**, *12*, 745–769.

(4) Rufford, T.; Smart, S.; Watson, G.; Graham, B.; Boxall, J.; Diniz da Costa, J.; May, E. The removal of CO_2 and N_2 from natural gas: A review of conventional and emerging process technologies. *J. Pet. Sci. Eng.* **2012**, *94-95*, 123–154.

(5) Hepburn, C.; Adlen, E.; Beddington, J.; Carter, E. A.; Fuss, S.; Mac Dowell, N.; Minx, J. C.; Smith, P.; Williams, C. K. The technological and economic prospects for CO_2 utilization and removal. *Nature* **2019**, *575*, 87–97.

(6) Pakhare, D.; Spivey, J. A review of dry (CO_2) reforming of methane over noble metal catalysts. *Chem. Soc. Rev.* **2014**, *43*, 7813–7837.

(7) Horn, R.; Schlögl, R. Methane Activation by Heterogeneous Catalysis. *Catal. Lett.* **2015**, *145*, 23–39.

(8) Fankhauser, S.; Smith, S. M.; Allen, M.; Axelsson, K.; Hale, T.; Hepburn, C.; Kendall, J. M.; Khosla, R.; Lezaun, J.; Mitchell-Larson, E.; Obersteiner, M.; Rajamani, L.; Rickaby, R.; Seddon, N.; Wetzer, T. The meaning of net zero and how to get it right. *Nat. Clim. Chang.* **2022**, *12*, 15–21.

(9) Gross, L.; Mohn, F.; Moll, N.; Liljeroth, P.; Meyer, G. The Chemical Structure of a Molecule Resolved by Atomic Force Microscopy. *Science* **2009**, *325*, 1110–1114.

(10) In this technique, a small amount of CO molecules is adsorbed on the surface of interest, and a single CO molecule is placed at the foremost part of the probe by picking it up from the surface.[9]

(11) Gross, L.; Schuler, B.; Pavliček, N.; Fatayer, S.; Majzik, Z.; Moll, N.; Peña, D.; Meyer, G. Atomic Force Microscopy for Molecular Structure Elucidation. *Angew. Chem. Int. Ed.* **2018**, *57*, 3888–3908.

(12) Giessibl, F. J. The qPlus sensor, a powerful core for the atomic force microscope. *Rev. Sci. Instrum.* **2019**, *90*, 011101.

(13) Zhong, Q.; Li, X.; Zhang, H.; Chi, L. Noncontact atomic force microscopy: Bond imaging and beyond. *Surf. Sci. Rep.* **2020**, *75*, 100509.

(14) Kichin, G.; Weiss, C.; Wagner, C.; Tautz, F. S.; Temirov, R. Single Molecule and Single Atom Sensors for Atomic Resolution Imaging of Chemically Complex Surfaces. *J. Am. Chem. Soc.* **2011**, *133*, 16847–16851.

(15) Gross, L.; Moll, N.; Mohn, F.; Curioni, A.; Meyer, G.; Hanke, F.; Persson, M. High-Resolution Molecular Orbital Imaging Using a p-Wave STM Tip. *Phys. Rev. Lett.* **2011**, *107*, 086101.

(16) Hapala, P.; Kichin, G.; Wagner, C.; Tautz, F. S.; Temirov, R.; Jelinek, P. Mechanism of high-resolution STM/AFM imaging with functionalized tips. *Phys. Rev. B* **2014**, *90*, 085421.

(17) Nguyen, G. D. et al. Atomically precise graphene nanoribbon heterojunctions from a single molecular precursor. *Nat. Nanotechnol.* **2017**, *12*, 1077–1082.

(18) Lawrence, J.; Sosso, G. C.; Đorđević, L.; Pinfold, H.; Bonifazi, D.; Costantini, G. Combining high-resolution scanning tunnelling microscopy and first-principles simulations to identify halogen bonding. *Nat. Commun.* **2020**, *11*, 2103.

(19) Lawrence, J.; Brandimarte, P.; Berdonces-Layunta, A.; Mohammed, M. S.; Grewal, A.; Leon, C. C.; Sánchez-Portal, D.; De Oteyza, D. G. Probing the Magnetism of Topological End States in 5-Armchair Graphene Nanoribbons. *ACS Nano* **2020**, *14*.

(20) Song, S. et al. Real-Space Imaging of a Single-Molecule Monoradical Reaction. *J. Am. Chem. Soc.* **2020**, *142*, 13550–13557.

(21) Song, S.; Su, J.; Peng, X.; Wu, X.; Telychko, M. *Molecular Interactions on Two-Dimensional Materials*; World Scientific, 2021; Chapter 8, pp 277–301.

(22) Li, J.; Sanz, S.; Merino-Díez, N.; Vilas-Varela, M.; Garcia-Lekue, A.; Corso, M.; de Oteyza, D. G.; Frederiksen, T.; Peña, D.; Pascual, J. I. Topological phase transition in chiral graphene nanoribbons: from edge bands to end states. *Nat. Commun.* **2021**, *12*, 5538.

(23) Martinez-Castro, J.; Bolat, R.; Fan, Q.; Werner, S.; Arefi, H. H.; Esat, T.; Sundermeyer, J.; Wagner, C.; Michael Gottfried, J.; Temirov, R.; Ternes, M.; Stefan Tautz, F. Disentangling the electronic structure of an adsorbed graphene nanoring by scanning tunneling microscopy. *Commun. Mater.* **2022**, *3*, 57.

(24) Sun, K.; Silveira, O. J.; Ma, Y.; Hasegawa, Y.; Matsumoto, M.; Kera, S.; Krejčí, O.; Foster, A. S.; Kawai, S. On-surface synthesis of disilabenzene-bridged covalent organic frameworks. *Nat. Chem.* **2023**, *15*, 136–142.

(25) Gross, L.; Mohn, F.; Moll, N.; Schuler, B.; Criado, A.; Guitian, E.; Peña, D.; Gourdon, A.; Meyer, G. Bond-Order Discrimination by Atomic Force Microscopy. *Science* **2012**, *337*, 1326–1329.

(26) Gross, L.; Mohn, F.; Liljeroth, P.; Repp, J.; Giessibl, F. J.; Meyer, G. Measuring the Charge State of an Adatom with Noncontact Atomic Force Microscopy. *Science* **2009**, *324*, 1428–1431.

(27) Mohn, F.; Gross, L.; Moll, N.; Meyer, G. Imaging the charge distribution within a single molecule. *Nat. Nanotechnol.* **2012**, *7*, 227–231.

(28) Mallada, B.; Gallardo, A.; Lamanec, M.; de la Torre, B.; pirko, V. A.; Hobza, P.; Jelinek, P. Real-space imaging of anisotropic charge of σ-hole by means of Kelvin probe force microscopy. *Science* **2021**, *374*, 863–867.

(29) de Oteyza, D. G.; Gorman, P.; Chen, Y.-C.; Wickenburg, S.; Riss, A.; Mowbray, D. J.; Etkin, G.; Pedramrazi, Z.; Tsai, H.-Z.; Rubio, A.; Crommie, M. F.; Fischer, F. R. Direct Imaging of Covalent Bond Structure in Single-Molecule Chemical Reactions. *Science* **2013**, *340*, 1434–1437.

(30) Albrecht, F.; Fatayer, S.; Pozo, I.; Tavernelli, I.; Repp, J.; na, D. P.; Gross, L. Selectivity in single-molecule reactions by tip-induced redox chemistry. *Science* **2022**, *377*, 298–301.

(31) Clair, S.; de Oteyza, D. G. Controlling a chemical coupling reaction on a surface: tools and strategies for on-surface synthesis. *Chem. Rev.* **2019**, *119*, 4717–4776.

(32) Zhou, J.; Acharya, D.; Camillone III, N.; Sutter, P.; White, M. G. Adsorption Structures and Electronic Properties of 1,4-Phenylene Diisocyanide on the Au(111) Surface. *J. Phys. Chem. C* **2011**, *115*, 21151–21160.

(33) Kestell, J.; Abuflaha, R.; Boscoboinik, J. A.; Garvey, M.; Bennett, D. W.; Tysoe, W. T. Determination of Adsorbate Structures from 1,4-Phenylene Diisocyanide on Gold. *J. Phys. Chem. Lett* **2014**, *5*, 3577–3581.

(34) Ghalgaoui, A.; Doudin, N.; Calaza, F.; Surnev, S.; Sterrer, M. Ordered Au Nanoparticle Array on Au(111) through Coverage Control of Precursor Metal-Organic Chains. *J. Phys. Chem. C* **2016**, *120*, 17418–17426.

(35) Feng, M.; Sun, H.; Zhao, J.; Petek, H. Self-Catalyzed Carbon Dioxide Adsorption by Metal-Organic Chains on Gold Surfaces. *ACS Nano* **2014**, *8*, 8644–8652.

(36) Feng, M.; Petek, H.; Shi, Y.; Sun, H.; Zhao, J.; Calaza, F.; Sterrer, M.; Freund, H.-J. Cooperative Chemisorption-Induced Physisorption of CO_2 Molecules by Metal-Organic Chains. *ACS Nano* **2015**, *9*, 12124–12136.

(37) In the absence of PDI molecules, the CO_2 nucleates preferentially at the middle of the terraces forming islands that exhibit a single domain (Figures S2 and S3), unless coalescence with other islands by the presence of nearby nucleation points takes place (Figure S2c and S2d). presence of dispersed PDI–Au chains captures the CO_2 molecules diffusing on the surface.

(38) Boscoboinik, J.; Kestell, J.; Garvey, M.; Weinert, M.; Tysoe, W. T. Creation of low-coordination gold sites on Au(111) surface by 1,4-phenylene diisocyanide adsorption. *Top. Catal.* **2011**, *54*, 20–25.

(39) Shiotari, A.; Sugimoto, Y. Ultrahigh-resolution imaging of water networks by atomic force microscopy. *Nat. Commun.* **2017**, *8*, 14313.

(40) Repp, J.; Meyer, G.; Stojković, S.; Gourdon, A.; Joachim, C. Molecules on Insulating Films: Scanning-Tunneling Microscopy Imaging of Individual Molecular Orbitals. *Phys. Rev. Lett.* **2005**, *94*, 026803.

(41) Stetsovych, O.; Todorovic, M.; Shimizu, T. K.; Moreno, C.; Ryan, J. W.; Leon, C. P.; Sagisaka, K.; Palomares, E.; Matolin, V.; Fujita, D.; Perez, R.; Custance, O. Atomic species identification at the (101) anatase surface by simultaneous scanning tunnelling and atomic force microscopy. *Nat. Commun.* **2015**, *6*, 7265.

(42) Bulou, H.; Massobrio, C. New atomic mechanism of preferential nucleation on the herringbone reconstruction of Au(111). *J. Phys. Chem. C* **2008**, *112*, 8743–8746.

(43) Ellner, M.; Pou, P.; Pérez, R. Molecular Identification, Bond Order Discrimination, and Apparent Intermolecular Features in Atomic Force Microscopy Studied with a Charge Density Based Method. *ACS Nano* **2019**, *13*, 786–795.

(44) Zahl, P.; Yakutovich, A. V.; Ventura-Macías, E.; Carracedo-Cosme, J.; Romero-Muñiz, C.; Pou, P.; Sadowski, J. T.; Hybertsen, M. S.; Pérez, R. Hydrogen bonded trimesic acid networks on Cu(111) reveal how basic chemical properties are imprinted in HR-AFM images. *Nanoscale* **2021**, *13*, 18473–18482.

(45) Ventura-Macias, E.; Romero-Muñiz, C.; González-Sánchez, P.; Pou, P.; Pérez, R. Are High Resolution Atomic Force Microscopy images proportional to the force gradient or the force maps? *Appl. Surf. Sci.* **2023**, *634*, 157558.

(46) Ellner, M.; Pou, P.; Pérez, R. In *Kelvin Probe Force Microscopy: From Single Charge Detection to Device Characterization*; Sadewasser, S., Glatzel, T., Eds.; Springer, 2018; pp 465–497.

(47) Weymouth, A. J.; Hofmann, T.; Giessibl, F. J. Quantifying molecular stiffness and interaction with lateral force microscopy. *Science* **2014**, *343*, 1120–1122.

(48) Bartels, L.; Meyer, G.; Rieder, K.-H.; Velic, D.; Knoesel, E.; Hotzel, A.; Wolf, M.; Ertl, G. Dynamics of Electron-Induced Manipulation of Individual CO Molecules on Cu(111). *Phys. Rev. Lett.* **1998**, *80*, 2004–2007.

(49) Albrecht, T. R.; Grütter, P.; Horne, D.; Rugar, D. Frequency modulation detection using high-Q cantilevers for enhanced force microscope sensitivity. *J. Appl. Phys.* **1991**, *69*, 668.

(50) Kresse, G.; Furthmüller, J. Efficient iterative schemes for *ab initio* total-energy calculations using a plane-wave basis set. *Phys. Rev. B* **1996**, *54*, 11169.

(51) Blöchl, P. E. Projector augmented-wave method. *Phys. Rev. B* **1994**, *50*, 17953.

(52) Perdew, J. P.; Burke, K.; Ernzerhof, M. Generalized Gradient Approximation Made Simple. *Physical Review Letters* **1996**, *77*, 3865–3868.

(53) Grimme, S.; Antony, J.; Ehrlich, S.; Krieg, H. A consistent and accurate *ab initio* parametrization of density functional dispersion correction (DFT-D) for the 94 elements H-Pu. *J. Chem. Phys.* **2010**, *132*, 154104.

(54) Hapala, P.; Temirov, R.; Tautz, F. S.; Jelinek, P. Origin of High-Resolution IETS-STM Images of Organic Molecules with Functionalized Tips. *Phys. Rev. Lett.* **2014**, *113*, 226101.

(55) Krejčí, O.; Hapala, P.; Ondráček, M.; Jelínek, P. Principles and simulations of high-resolution STM imaging with a flexible tip apex. *Phys. Rev. B* **2017**, *95*, 045407.

(56) Tersoff, J.; Hamann, D. R. Theory of the scanning tunneling microscope. *Phys. Rev. B* **1985**, *31*, 805–813.

(57) Chen, C. J. Tunneling matrix elements in three-dimensional space: The derivative rule and the sum rule. *Phys. Rev. B* **1990**, *42*, 8841–8857.

(58) Chen, C. J. Theory of scanning tunneling spectroscopy. *J. Vacuum Sci. Technol. A* **1988**, *6*, 319–322.

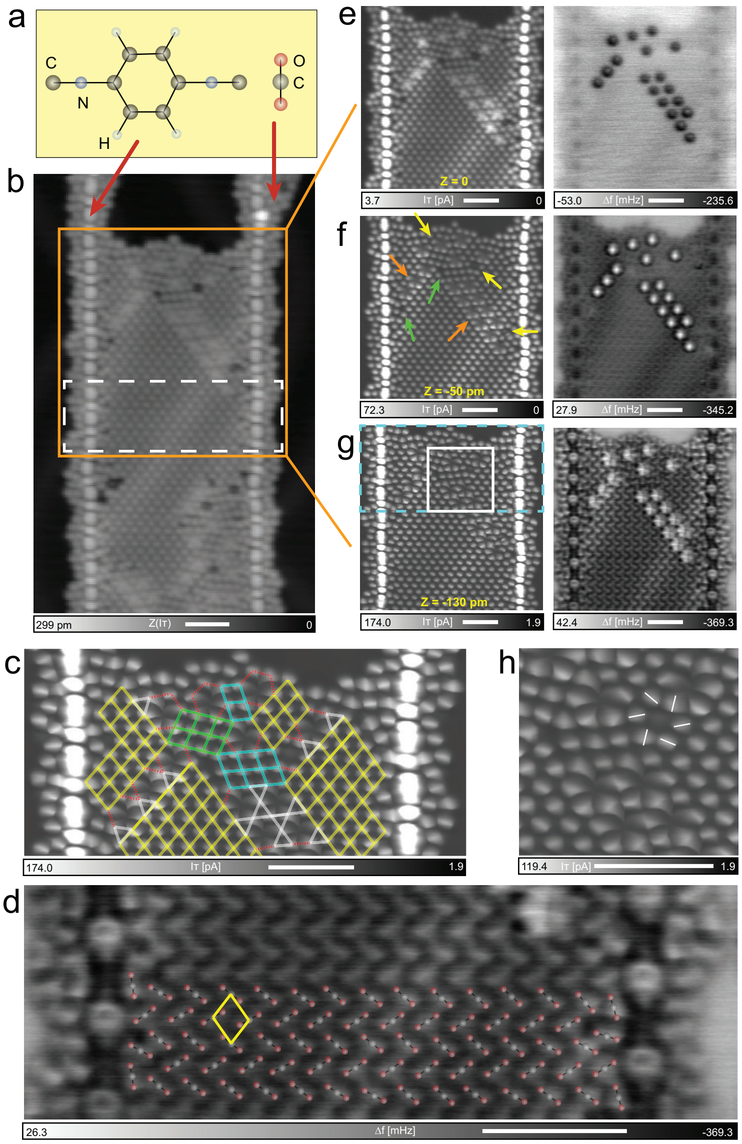

Figure 1: (a), Chemical structure of the PDI and the CO_2 molecules. (b), STM image of CO_2 molecules confined between two PDI–Au chains. The sample bias voltage (V) and tunneling current (I_T) set-point are 105 mV and 5 pA, respectively. (c), Constant-height current signal of the area enclosed by the rectangle in (g) featuring rhombic and triangular configurations of CO_2 molecules. Dotted red lines indicate hexagonal structures. (d), Constant-height AFM (Δf) image of the area enclosed by a rectangle in (b) acquired using an oscillation amplitude (A) of 75 pm and a free oscillation resonant frequency (f_0) of 999646 Hz. Diagrams of CO_2 molecules and a single rhombic cell have been superimposed. (e) to (g), Series of height-dependent simultaneously acquired constant-height I_T and Δf images measured over the region highlighted with a square in (b) by approaching the probe towards the surface from the separation (Z= 0) corresponding to the imaging conditions in (b). The I_T contrast has been saturated over the PDI-Au chains to display the details of the confined CO_2 layer. Green, orange and yellow arrows in (f) point towards voids and two types of defects in the molecular layer. (h), Zoom-in on the region marked by a square in (g). Lines highlight the windmill-like arrangement of the CO_2 molecules enclosing the defect pointed by the top-right yellow arrow in (f). The scale bar corresponds to a 2 nm length.

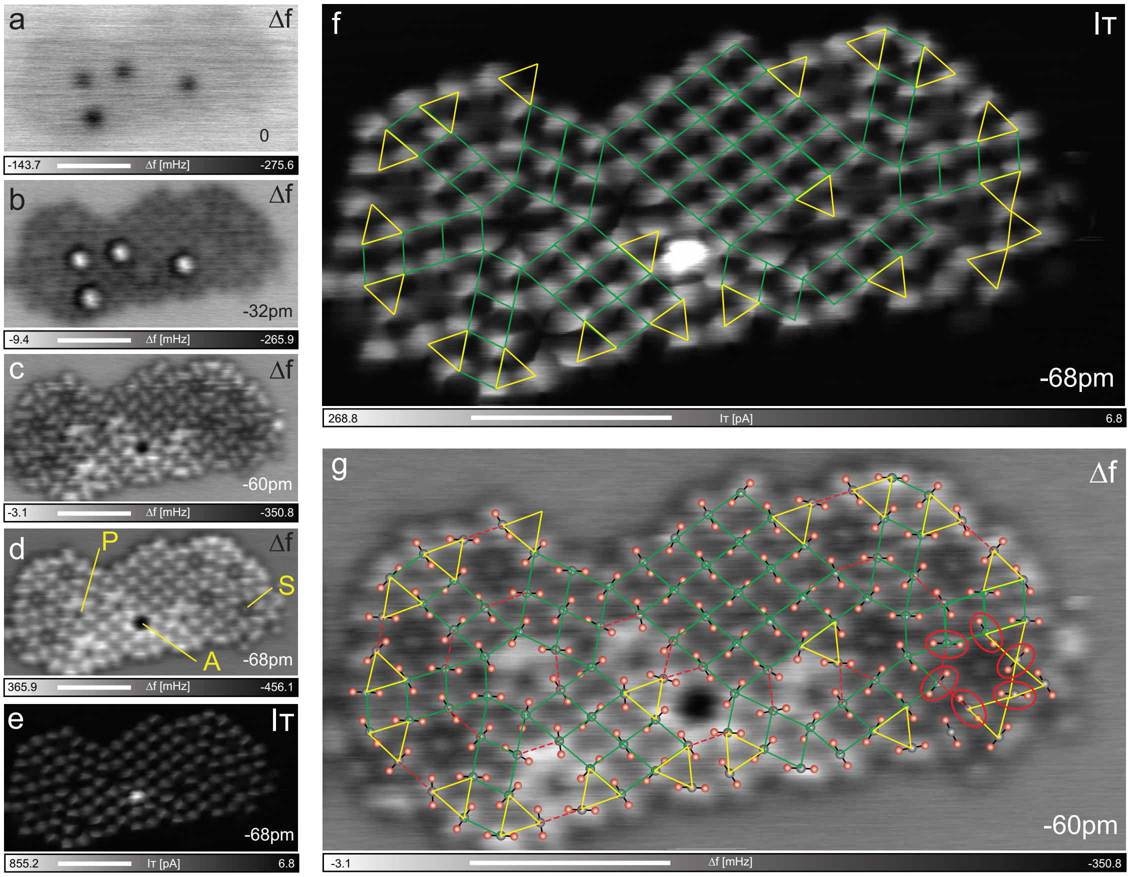

Figure 2: (a) to (d), Selection of AFM frames from a series of height-dependent simultaneously acquired STM (I_T) and AFM (Δf) images over an island of CO_2 molecules that exhibits the three types of defects also found at the CO_2 layers confined between PDI–Au chains. These defects are labelled A, S and P in (d). (e), STM image at the closest approach during the series. (f), and (g), Structural analysis of the CO_2 molecular arrangements in (e) and (c), respectively. The signal in (f) has been saturated over the defect A to enhance the contrast over the CO_2 molecules. Green lines mark rhombic domains of CO_2 molecules, and yellow triangles denote CO_2 molecules exhibiting a triangular arrangement. In (g), the CO_2 structure has been superimposed over each molecule to highlight its orientation. The red dashed lines close the hexagonal patterns that enclose the defects. The red ovals highlight CO_2 molecules in a windmill-like configuration. The separation at which each image was acquired during the series labels each frame. Image size and acquisition parameters are: (8×4) nm^2, A = 75 pm, f_0 = 999646 Hz, V = 5 mV. The scale bar corresponds to a 2 nm length. A movie showing the images acquired for the whole series is available in the Supporting Information.

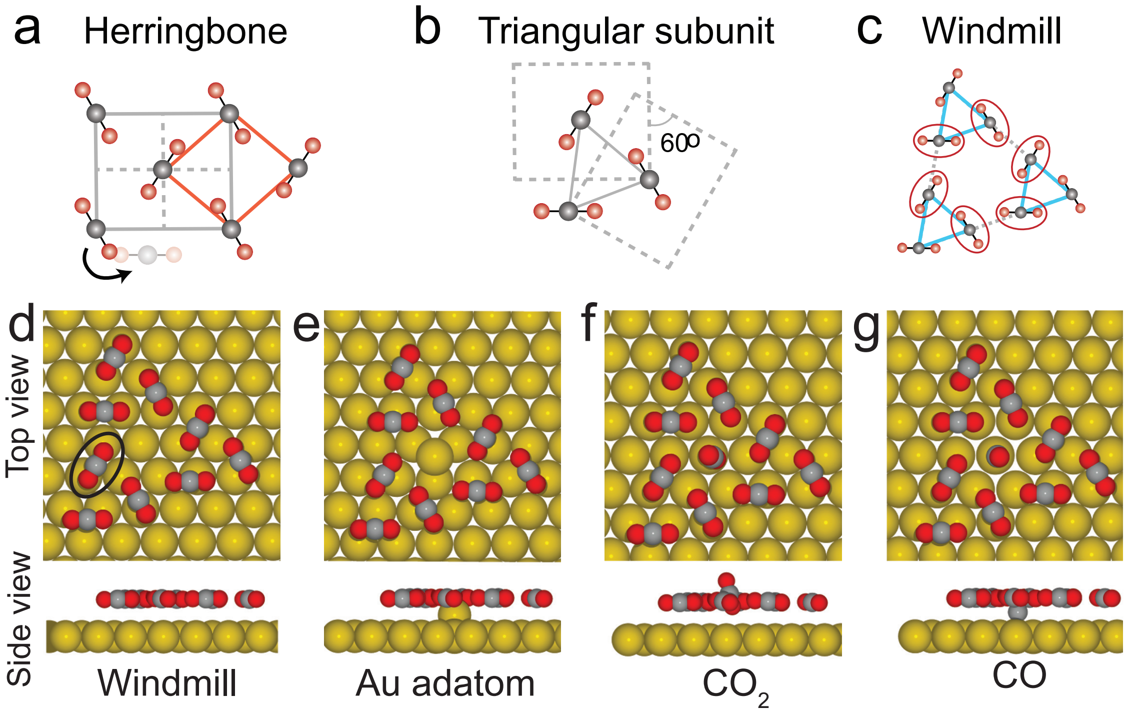

Figure 3: (a), Close-packed herringbone structure of the CO_2 molecules with the orthorhombic (grey) and rhombic (red) unit cells. (b), Triangular subunit formed by rotating two herringbone unit cells 60°. The displacement and rotation of the molecule highlighted with an arrow in (a) produces this subunit. (c), Windmill structure combining three triangular subunits. The ovals highlight the molecules that form the windmill structure detected in the experiments. Top and side views of the DFT calculated structures for: (d), an empty windmill; (e), a gold adatom over the gold surface enclosed by a windmill; (f), a CO_2 molecule adsorbed in a vertical configuration inside a windmill; and (g), a CO molecule adsorbed on the gold surface inside a windmill. The oval in (d) marks the molecule also highlighted in Figures 4a to 4d.

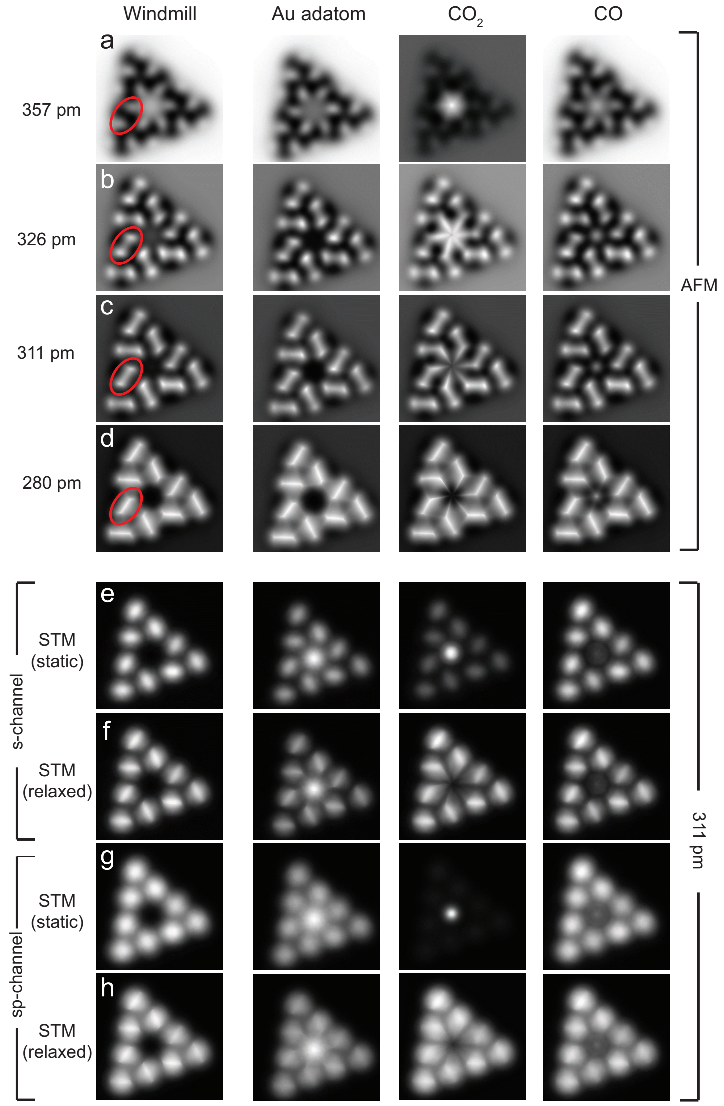

Figure 4: Simulated AFM and STM images of the defects enclosed by windmill structures observed in the experiments. (a) to (d), AFM images for four representative probe-layer separations (357 pm, 326 pm, 311 pm, and 280 pm) using an oscillation amplitude of 70 pm. The red ovals in (a) to (d) mark the same CO$_2$ molecule of the windmill. (e) to (h), STM images for a 311 pm separation. The rows of images labelled as *s–channel* in (e) and (f) are calculated considering only the contribution of the 5σ CO orbital to the tunneling current. The rows of images labelled as *sp–channel* in (g) and (h) take into account the contribution of both the 5σ and the 2π^* orbitals of the CO (represented by the s and the p_x, p_y orbital channels, see Methods). The rows displaying the label (*relaxed*) show images including the relaxation of the CO at the probe, in contrast to the images calculated assuming a static CO, labelled as (*static*). The distances are measured from the oxygen atom of the CO probe in a vertical position to the plane of the CO$_2$ layer. The defects follow the same order and labelling as in Figure 3. Image contrast scales for the AFM images are shown in Figure S6.

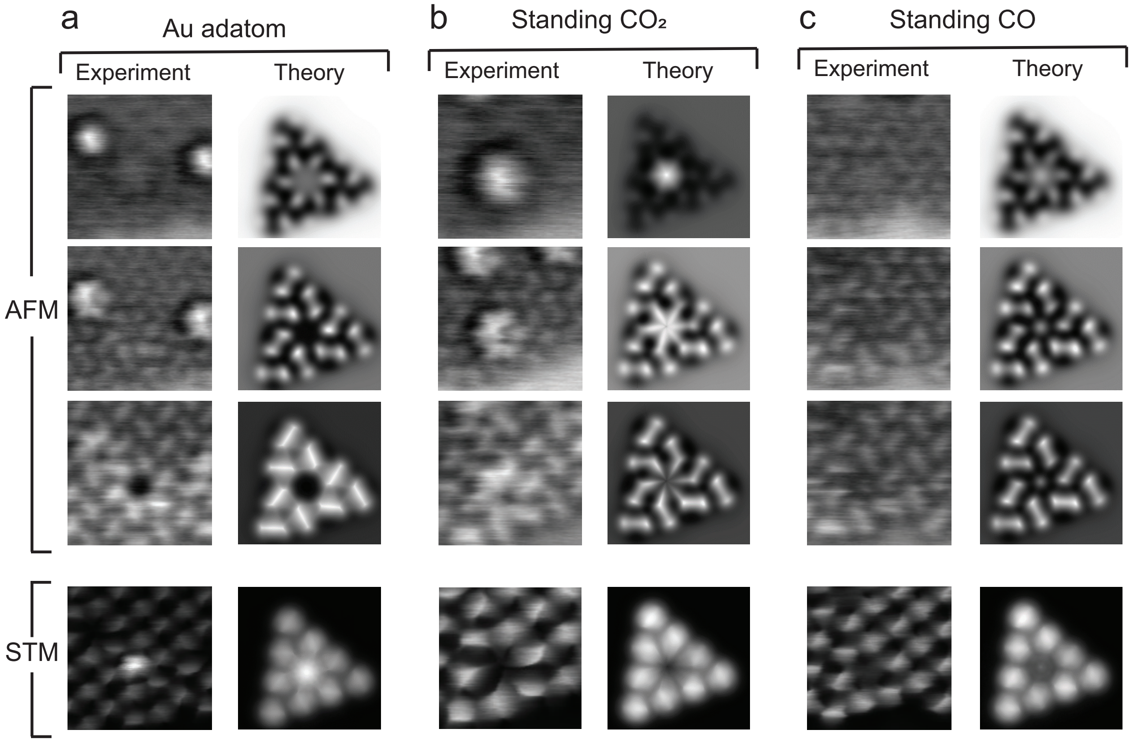

Figure 5: Side-by-side comparison of the main features obtained from both experimental (Figures 1 and 2) and calculated (Figure 4) AFM and STM images for windmill structures of CO_2 molecules enclosing: (a), a gold adatom; (b), a standing CO_2 molecule; and (c), a standing CO molecule.

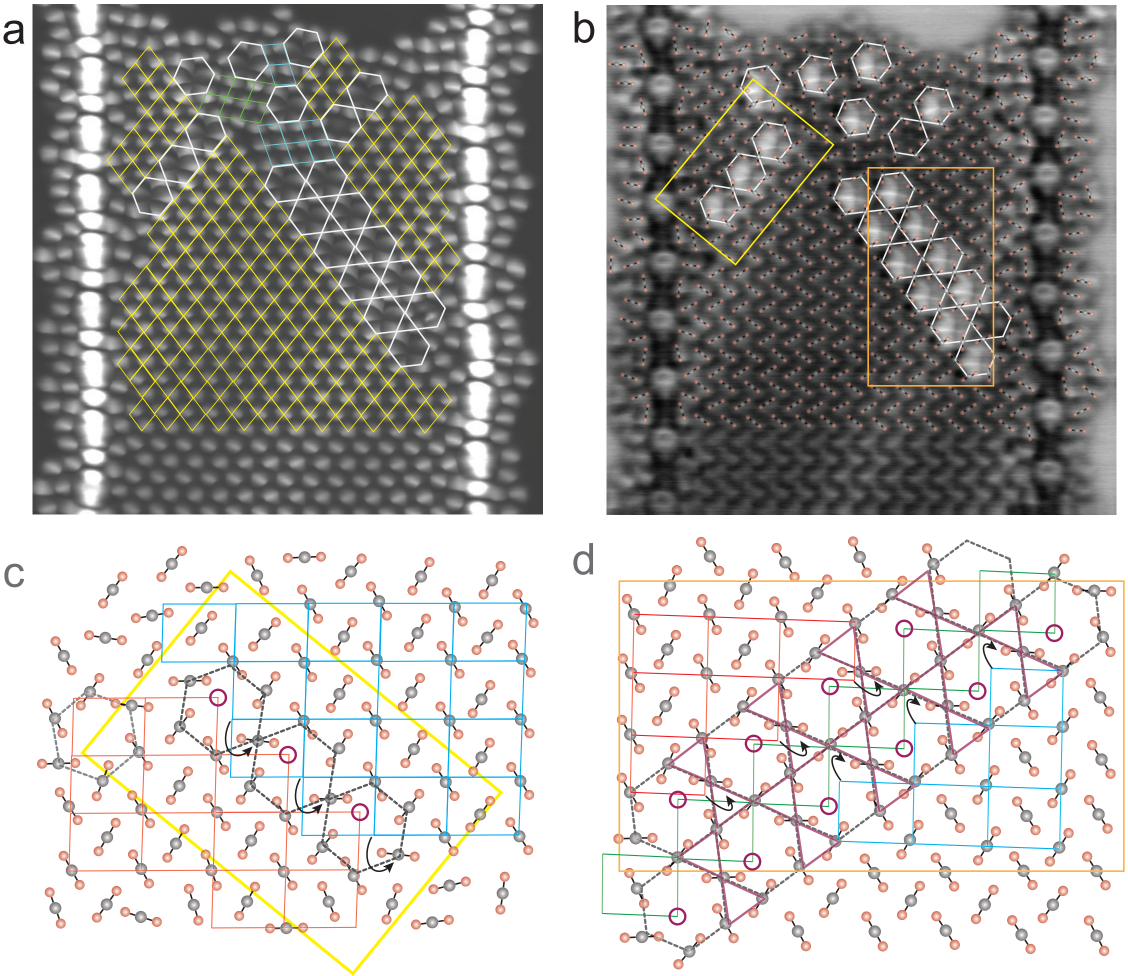

Figure 6: (a) and (b), STM and AFM images displayed in Figure 1 g. Rhombic lattices in yellow, cyan and green highlight translational and rotational domains of CO_2 molecules. Ball-and-stick models of the CO_2 molecule have been superimposed to the corresponding AFM signal to highlight the molecular orientation. White hexagons mark the position of the windmill structures. (c), Detail of the molecular arrangement enclosed by the yellow rectangle in (b). (d), Detail of the molecular arrangement enclosed by the orange rectangle in (b). Lines in cyan, red and green mark the unit cells of different translational domains of the CO_2 molecules. In panel (d), the lines in magenta highlight the formation of triangular structures by the displacement and rotation (indicated by arrows) of the CO_2 molecules from the rhombic domains. Dashed grey lines represent the position of the windmill structures depicted in (a) and (b). Circles in magenta indicate the possible origin of the standing CO_2 molecules populating the windmills (these standing CO_2 molecules are not included in (c) and (d) for clarity). The models for the CO_2 molecules correspond with the position of the molecules detected in (b).